Vat Photopolymerization 3D Printing of Hydrogels Embedding Metal–Organic Frameworks for Photodynamic Antimicrobial Therapy

Original
Vat Photopolymerization 3D Printing of Hydrogels Embedding Metal–Organic Frameworks for Photodynamic Antimicrobial Therapy / Wang, Y., Frascella, F., Gaglio, C.G., Pirri, C., Wei, Q., Roppolo, I.. - In: ACS APPLIED MATERIALS & INTERFACES. - ISSN 1944-8252. - ELETTRONICO. - 16:42(2024), pp. 57778-57791. [10.1021/acsami.4c15168]

Publisher:
American Chemical Society

Published
DOI:10.1021/acsami.4c15168

Vat photopolymerization 3D printing of hydrogels embedding metal-organic frameworks for photodynamic antimicrobial therapy

Yang Wang [a], Francesca Frascella [b], Cesare Gabriele Gaglio [b], Candido Fabrizio Pirri [b], Qufu Wei [a, *], Ignazio Roppolo [b, *]

[a] Key Laboratory of Eco-textiles of Ministry of Education, College of Textile Science and Engineering, Jiangnan University, Wuxi, Jiangsu 214122, China

[b] Department of Applied Science and Technology, Politecnico di Torino, Duca degli Abruzzi, 24, 10124 Torino, Italy

*Correspondence to: Ignazio Roppolo (ignazio.roppolo@polito.it), Qufu Wei (qfwei@jiangnan.edu.cn)

Abstract: Given the variability in wounds based on the underlying causes, personalized medicine and tailored care for patients with wounds are required to ensure optimal therapeutic outcomes. With the emergence of high-precision and high-efficiency photocuring 3D printing technology, there is the potential for its use in customizing precise shapes that can match complex wound sites, thereby providing better treatment for patients with wound infections. In this work, porphyrinic metal-organic frameworks (MOF) crystals, serving as the functional filler, were incorporated into gelatin methacrylate (GelMA) as a photocurable composite resin to investigate the capabilities of producing customizable wound dressings through vat photopolymerization 3D printing. The embedded MOF crystals allow for better control of the photopolymerization process due to photon competition with the photoinitiator, enabling the precise printing of complex structures. In addition, these crystals impart photothermal and photodynamic capabilities to the printed object. The antibacterial assay confirms the potent photothermal/photodynamic bactericidal properties of the printed GelMA/MOF hydrogels. The hydrogel with the highest MOF content exhibited over 99.99% antibacterial efficiency against both *Gram-positive Staphylococcus aureus* and *Gramnegative Escherichia coli* after 30 min of light exposure (~30 mW/cm^2, $\lambda \geq 420$ nm). Simultaneously, hemolysis and cytotoxicity evaluations validated their excellent biocompatibility. The findings presented here introduce a strategy for integrating photosensitive MOF and 3D printing to fabricate size-adjustable photothermal/photodynamic monoliths and patches, opening perspectives towards personalized treatment for wound management.

Keywords: GelMA, porphyrinic MOF, vat photopolymerization 3D printing, photothermal, photodynamic

1. Introduction

Over the years, wound infection has posed a major threat to human health due to the heightened vulnerability of injured skin to bacterial invasion and proliferation [1]. To address this issue, a substantial number of antibiotics have been developed and implemented for practical applications [2]. However, conventional antibiotics are becoming less effective due to the emergence of antibiotic-resistant strains resulting from their common misuse and overuse [3]. Therefore, alternative approaches that can effectively face bacterial infections are urgently needed. Recently, photodynamic therapy (PDT) has emerged as a promising strategy, which can inactivate pathogens by generating reactive oxygen species (ROS) through photochemical reactions. Importantly, ROS sterilize the bacteria by disrupting the cell membrane structure, thereby mitigating the concern of bacterial resistance [4,5].

Currently, an increasing number of materials have been demonstrated to produce ROS for achieving PDT, such as carbon quantum dots (CQDs), molybdenum disulfide (MoS_2), and metal-organic framework (MOF) [6-8]. Among them, MOF coordinated by organic linkers and metal nodes is an emerging class of photodynamic materials with ultrahigh porosity [9]. In particular, porphyrinic MOF possesses not only exceptional photodynamic effects but also excellent photothermal performance, making them have great potential in clinical therapeutics [10]. Numerous studies on porphyrinic MOF for chronic wounds, ophthalmic, and even oral treatments have been reported recently [11-13]. However, such nano-sized solids are not suitable for direct use in the human body due to the leakage and residual hazards, and apparently some reports on medical

MOF have ignored this crucial consideration. Fortunately, encapsulating and immobilizing MOF within hydrogel systems seems to be a feasible strategy. For instance, Gwon et al. employed diacrylated polyethylene glycol and 4-arm-thiolated PEG as the photocuring matrix to fabricate bioactive MOF-embedded hydrogels. These hydrogels can kill bacteria by the slow release of metal ions through the degradation of embedded MOF [14]. Huang et al. also reported a multifunctional composite hydrogel, which encapsulated modified curcumin-based MOF for chronic wound management [15]. Although these studies have highlighted the great potential of MOF-based hydrogels in wound dressings, building complex shapes and conformable patches to closely match the skin defects is also of significant importance for clinical needs [16]. Specifically, each patient's wound is distinct, differing in size, depth, location, and severity [17]. Tailoring the dressing to the specific characteristics of the wound could ensure optimal coverage and contact with the affected area, promoting effective healing [18]. Therefore, here we propose to employ Digital Light Processing (DLP) 3D printing technology to fabricate MOF-loaded hydrogels, aiming to satisfy the personalized antimicrobial treatment of different-shape wounds.

DLP is a precise and efficient additive manufacturing (AM) technique that employs a projector-based system to selectively cure photosensitive resins layer by layer, enabling to create complex three-dimensional (3D) objects [19, 20]. Notably, compared to other 3D printing techniques, DLP offers unique advantages such as higher printing resolution and accuracy, faster speed, and smoother surface finish [21, 22]. In healthcare, DLP 3D printing enables the rapid production of wound dressings customized to specific shapes, which is especially crucial during emergencies when there is a sudden surge in patient demands. Furthermore, it may be compatible with the embedding of electronic components during the manufacturing process, facilitating the development of smart medical devices or dressings with real-time monitoring, diagnostic, and even therapeutic functions[23,24]. However, there has been limited research on DLP printed hydrogel dressings for wound therapy. Up to now, many reports have increasingly indicated that DLP is an outstanding strategy for fabricating hydrogels with complex 3D shapes employing both synthetic and natural raw materials [25-30]. Among different categories of bio-based hydrogel photocurable materials, gelatin methacrylate (GelMA) has been widely used in tissue engineering, wound repair, and drug release system because of its excellent biocompatibility and photopolymerizable characteristics [31-33]. The high optical transparency of GelMA hydrogels can provide good light transmission for the embedded photosensitizers to initiate photochemical reactions, as demonstrated by several publications [34-37].

In this study, a porphyrinic MOF (PCN-224) composed of Zr-oxo clusters and 5,10,15,20-tetrakis (4-carboxyphenyl) porphyrin (H_2TCPP) ligands was chosen as the filler for the DLP 3D printing [38]. PCN-224 has been widely utilized as a PDT agent due to its advantages of efficient diffusion of ROS, great chemical/physical stability, and high biocompatibility [38-40]. To the best of our knowledge, it’s the first time that porphyrinic MOF are employed as functional fillers in this advanced technology. Briefly, different concentrations of this MOF were incorporated into GelMA matrix to fabricate GelMA/MOF hydrogels using a DLP 3D printer. Taking into account the light-absorption of the MOF, those can be used as smart dyes, able to improve printing precision and impart functional properties to the objects [41]. Consequently, the curing behavior of the GelMA/MOF formulations was measured by photorheology and printing parameters were optimized to fabricate complex shape structures. The printed GelMA/MOF hydrogels were systematically characterized by morphological observation, water retention, swelling and mechanical properties. The photothermal and photodynamic characterizations of GelMA/MOF hydrogels were also performed. In addition, the antibacterial efficiency of the GelMA/MOF hydrogels against Gram-positive *Staphylococcus aureus* (*S. aureus*) and Gram-negative *Escherichia coli* (*E. coli*) was evaluated under visible light (~30 mW/cm^2, $\lambda \geq 420$ nm). The hemolysis and cytotoxicity assays were conducted to assess the hemocompatibility and cytocompatibility, respectively. All these findings indicated that this strategy enables the customization of dressings to match the specific contours of the wound, ensuring optimal contact with the wound surface and thereby achieving effective photothermal/photodynamic therapy.

2. Experimental

2.1 Materials

The gelatine (Gel) used as precursor of gelatine methacrylate (GelMA) is Type B gelatin from bovine skin, Bloom 50-120 bought from Merck, Italy. Four types of GelMA type B (DS: 60%, 80%, 90%, 95%) were lab-synthesized following the procedures previously reported [33, 42-45]. $ZrOCl_2 \cdot 8H_2O$ (99.9%), 5,10,15,20-Tetrakis(4-

carboxyphenyl)porphyrin (TCPP, 97%), benzoic acid (99.5%) and 1,3-Diphenylisobenzofuran (DPBF) were purchased from Macklin Biochemical Technology, China. Water-soluble diphenyl (2,4,6-trimethylbenzoyl)phosphine oxide (TPO-SDS) and other chemicals were obtained from Merck, Italy. All chemicals were used as obtained without further purification.

2.2 Synthesis of MOF (PCN-224) nanoparticles

PCN-224 nanoparticles were synthesized according to previous method [38]. In brief, 1.5 g of benzoic acid and 0.15 g of $ZrOCl_2{\cdot}8H_2O$ were dissolved in 10 mL DMF under ultrasonication, then 0.05 g of TCPP was added in the DMF with continuous ultrasonication. After that, the mixture was transferred in a Pyrex vial and heated at 120 °C for 24 h. After the reaction, the mixture was naturally cooled to room temperature and centrifuged (8000 rpm/min, 30 min) to obtain the precipitated product. Subsequently, the product was washed with DMF twice and ethanol three times to remove impurities. Finally, PCN-224 nanoparticles were collected after drying in a vacuum oven at 60 °C for 12 h.

2.3 Formulations

GelMA/MOF formulations containing different concentrations (0.125, 0.25, 0.5, 1 mg/mL) of MOF nanoparticles were prepared, the notation used was $GelMA/MOF_x$ where x represents the concentration of MOF in the formulation. In detail, TPO-SDS (5% to GelMA, w/w) and GelMA were dissolved in deionized water (DI water) under ultrasonication to obtain GelMA precursor solution (30%, w/v). Then, MOF nanoparticles were ultrasonically dispersed in DI water at different concentrations

(0.25, 0.5, 1, 2 mg/mL). Afterward, equal volumes of the GelMA precursor solution and each MOF dispersion were mixed and vigorously stirred to obtain pre-printed GelMA/MOF formulations. The GelMA precursor solution was mixed with an equal volume of DI water to prepare pre-printed GelMA formulations, the final tested concentrations were: 10%, 12.5%, 15% and 20% w/v.

2.4 3D printing process

The printing process of the formulations was carried out with the DLP 3D printer (Asiga UV MAX27, Asiga, AUS) to fabricate GelMA and GelMA/MOFs hydrogels. Before the printing, various shapes of models were created using Cinema 4D software and converted in STL format.

Preliminary tests were carried out to assess light intensity and layer thickness. The formulations were dropped on a vat and exposed for different times under LED light with 40 mW/cm^2 intensity. Then, the formulations were exposed for a fixed time to different light intensities to investigate the relationship between light intensity and layer thickness.

The light intensity and the exposure time of each formulation was selected based on these results; briefly, the slice thickness was settled as 0.2 mm. After the printing process, each sample was carefully washed by 50 °C DI water to remove uncured formulations and then post-cured for 2 min in a UV chamber. For sterilization, the post-cured hydrogels were immersed in 70% ethanol for 1 h and kept in sterile phosphate buffered solution (PBS) at 4 °C.

2.5 Characterization

The morphology of synthesized MOF was observed by a transmission electron microscope (TEM, JEM-2100, Japan), and the average diameters and size distributions of MOF were measured by using Nano Measurer (China). The crystal structure of MOF was characterized by X-ray diffractometer (XRD, D2 PHASER, Germany), and the scanning angle was ranged from 2° to 40° with a step size of 2°/min. NEXUS 470 spectrometer (USA) was employed to record the Fourier transform infrared spectroscopy (FTIR). Photorheological measurements were performed using a rheometer (Physica MCR 302, Austria) with a broad band UV-light source (Hamamatsu LC8 lamp, Japan) at light intensity of 45 mW/cm^2. The morphologies of printed GelMA and GelMA/MOF hydrogels were characterized by a field emission scanning electron microscope (FESEM, Regulus8100, Japan). The UV-vis spectra were measured by a BioTek Synergy HTX Multimode Reader (USA). The mechanical property of printed hydrogels was tested by using dynamic mechanical analysis (DMA, METTLER TOLEDO DMA 1, Switzerland). All cylindrical hydrogels ($\Phi = 10$ mm, $H = 6$ mm) were carried out in compression mode (Displacement = 0.05 mm, Frequency = 10 Hz) at 25 °C and 37 °C. The ASIGA 3D-printer (Max-UV27, Alexandria, AUS) was employed for DLP 3D printing process, the printer employs a light source of 385 nm and has a nominal X-Y resolution of 27 × 27 μm^2. A 3D optical scanner (E3, 3Shape, Denmark) was utilized to evaluate print resolution.

2.6 Swelling and water retention tests

The swelling behavior and water retention of the printed hydrogels were measured according to pervious methods with slight modifications [46, 47]. For the swelling behaviors, the printed cube sample (4 × 4 × 4 mm^3) was freeze-dried to obtain a dry weight (W_0). Then, the lyophilized samples were transferred to PBS solution and incubated in 37 °C water for 48 h. At every interval, the sample was carefully wiped with filter paper and weight as (W_t). The swelling rate was calculated according to Eq. (1):

$$Swelling\ ratio\ (\%) = \frac{W_t - W_0}{W_0} \times 100 \qquad (1)$$

Regarding the water retention test, a cube sample (4 × 4 × 4 mm^3) was immersed in PBS for 24 h, then the sample was carefully wiped with filter paper to remove the excess moisture and weight as (W'_0). The sample was placed at room temperature (humidity: around 40%) and weighed it at different intervals (W'_t). The water retention was calculated according to Eq. (2):

$$Water\ retention\ (\%) = \frac{W'_t}{W'_0} \times 100 \qquad (2)$$

2.7 Degradation test

The degradation test was conducted according to a reported method [48]. In brief, the freeze-dried hydrogels were added into pre-weighted plastic bottles (W_b) and subsequently re-weighed (W_0). Then, 4 mL of PBS were added into each bottle and the specimens were incubated at 37 °C. At intervals of 1, 4, 8, 15, and 30 days, the liquid in the corresponding bottles was removed and the bottles were dried in a vacuum oven. The dried bottles were weighed (W_1) and the degradation percentage (D) was calculated using the Eq. (3):

$$D\ (\%) = \frac{W_1 - W_b}{W_0 - W_b} \times 100 \qquad (3)$$

2.8 Singlet oxygen ($^1O_2$) generation detected by DPBF

DPBF was used as a specific probe to detect the $^1O_2$ generation. Briefly, 4 mL of 50% ethanol containing DPBF (30 mg/L) was added to a plastic tube, then a printed cylindrical sample (Φ = 10 mm, H = 1 mm) was added in the bottom of this tube and keep in the dark for 1 h. After that, this tube was exposed to an illumination (520 nm laser) for 5 min. 200 μL of the solution in this tube was pipetted in a 96 well-plate and the UV-vis spectrum was recorded with a microplate reader every 1 min; in addition, the solution after each measurement was pipetted back into the tube for the next exposure.

2.9 Antibacterial efficiency and SEM images of bacterial morphology

The biocidal efficacy of printed GelMA and GelMA/MOF hydrogels against *S. aureus* (ATCC 6538) and *E. coli* (ATCC 43895) were evaluated by a modified AATCC 100-2004 Test [49, 50]. In detail, the sterile samples (Φ = 10 mm, H = 1 mm) were respectively placed on the bottom of a sterile 24-well plate, and 10 μL of bacterial suspension (10^6 colony-forming units/mL) was inoculated on each sample. Then, a Xenon lamp (~30 mW/cm^2, $\lambda \geq 420$ nm) illuminated each sample for 30 minutes at a vertical height. Meanwhile, the same samples were tested in another 24-well plate under darkness. Afterwards, 1 mL PBS was added to each well and vortexed for 30 s to suspend bacteria, then the bacterial suspension was diluted serially 3 times (10, 100, 1000-fold) and 50 μL of the dilution was evenly dropped on agar plates. After incubation at 37 °C for 16-24 h, the bacterial colonies on agar plates were counted. All the biocidal experiments were carried out in triplicate.

2.10 Hemolysis and Cytotoxicity assays

The hemolysis assay was conducted according to a previous method [51]. In detail, 5 mL of anticoagulant whole blood was added to 10 mL of PBS solution and centrifuged at 1500 rpm for 10 min to collect the underlying red blood cells (RBCs). Then the obtained RBCs were injected in PBS to prepare 5% (v/v) RBCs/PBS dilution. Afterwards, 0.5 mL of RBCs/PBS dilution was mixed with 1 mL of DI water or PBS and incubated for 3 h to establish the positive or negative group. Meanwhile, 0.5 mL of RBCs/PBS dilution was added to 1 mL of PBS containing 10 mg of freeze-dried GelMA or GelMA/MOF hydrogels, and co-incubated for 3 h to establish the experiment groups. These mixtures were centrifuged at 2000 rpm for 10 min after the incubation, and the absorbance of each supernatant was recorded by using a UV-vis spectrophotometer. The hemolysis ratio was calculated by Eq. (4):

$$Hemolysis\ ratio\ (\%) = \frac{A_{hydrogel} - A_{negative}}{A_{positive} - A_{negative}} \times 100 \qquad (4)$$

where $A_{positive}$, $A_{negative}$, and $A_{hydrogel}$ represent the absorbance of positive, negative, and freeze-dried hydrogel groups at 540 nm, respectively.

The *in vitro* cytotoxicity of printed GelMA and GelMA/MOF hydrogels was performed by CCK-8 assay method using mouse fibroblast cells (L929) [52]. Briefly, the L929 cells were revived in Dulbecco's Modified Eagle Medium (DMEM) under a 5% CO_2 atmosphere at 37°C, subsequently seeded in a 96-well plate and cultured for 24 h. Meanwhile, 10 mg of sterile hydrogel samples were incubated in DMEM at 37°C for 24 h to obtain the sample extracts. Afterward, the culture medium in the 96-well plate was aspirated and replaced with an equivalent volume of sample extracts. In addition, the 0.1% Triton X-100 was used as the positive control and DMEM as the negative control. The plate was then incubated for an additional 48 hours. The absorbance of the cell culture medium was measured at 450 nm after the addition of CCK-8 reagent. The cell viability of hydrogel samples was calculated by Eq. (5):

$$Cell\ viability\ (\%) = \frac{OD_{sample} - OD_{positive}}{OD_{negative} - OD_{positive}} \times 100 \qquad (5)$$

where $OD_{positive}$, $OD_{negative}$, and OD_{sample} represent the absorbance of positive control, negative control, and hydrogel sample groups, respectively.

2.11 Statistical analysis

The statistical analysis employed ANOVA and Student’s t-test. All experimental data were presented as mean ± standard deviation, with statistical significance determined at $P < 0.05$. The standard deviations in all figures were represented by error bars.

3. Results and discussions

3.1. Synthesis and characterization of MOF

The FESEM and TEM images in Fig. 1a illustrate the synthesis of MOF particles, which exhibit a predominantly spherical crystal morphology with an average diameter of approximately 158 nm and a size range spanning from 77 to 257 nm. The chemical and physical structures of the synthesized MOF were characterized by FTIR and XRD, respectively. As shown in FTIR spectrum (Fig. 1b), the peak around 1650 cm^{-1}, 1600 cm^{-1}, and 1415 cm^{-1} were ascribed to C=O stretching vibration, C=C stretching vibration and C-N bending vibration, respectively [3]. The XRD pattern exhibited several strong peaks around 4.6°, 6.4°, 7.9°, 9.1°, 11.2° and 13.7°, corresponding to the (002), (022), (222), (004), (224), and (006) crystal facets of PCN-224, respectively [53]. The results of FTIR and XRD characterizations are consistent with previous reports, confirming the successful synthesis of MOF (PCN-224) nanoparticles [50].

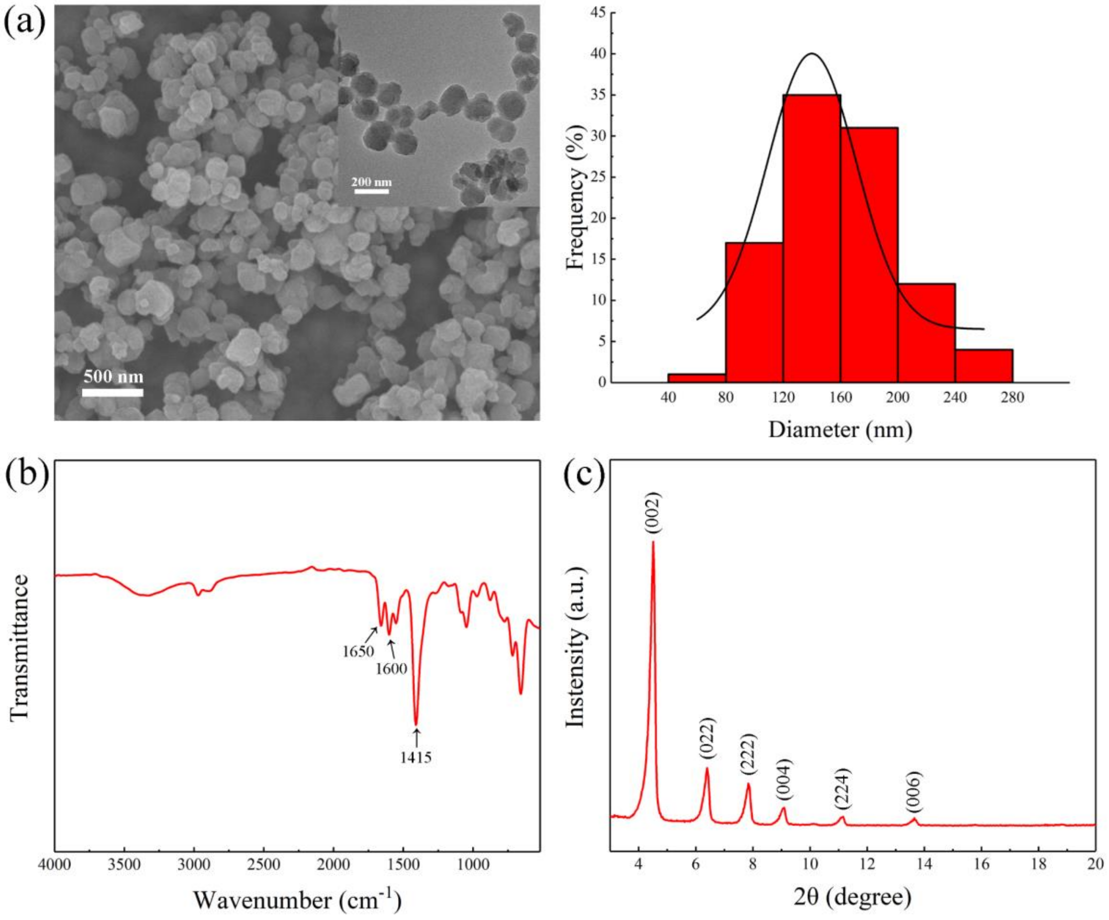

Fig. 1. (a) Morphology images and diameter distribution of the synthesized MOF. (b) FTIR spectrum of MOF. (c) XRD patterns of MOF.

3.2. Formulation design

In preliminary experiments, GelMAs with different degrees of methacrylation (60%, 80%, 90%, and 95%) were used to print cubic hydrogels. Each type of GelMA was printed at different concentrations of 10%, 12.5%, 15%, and 20% w/v in PBS or DI water. As shown in Fig. S1 in Supporting Information file, the GelMA formulations at low concentrations (10% and 12.5%) exhibited problematic cubes' printing, while the high concentration (20%) adversely affected the transparency. In contrast, the GelMA hydrogels with a concentration of 15% displayed better printability and transparency. Especially GelMA with a methacrylate substitution degree of 90% (GelMA$_{90}$) showed the best printing result. Therefore, GelMA$_{90}$ at a concentration of 15% was used as the polymer matrix for the preparation of GelMA/MOF formulations.

The schematic illustration of GelMA/MOF hydrogel formation mechanism is depicted in Fig. 2a. After exposure to UV light, the GelMA molecules are covalently crosslinked, forming a dense and stable gel network that encapsulates MOF nanoparticles. Fig. 2b exhibits the GelMA and GelMA/MOF formulations and the corresponding hydrogels. Obviously, GelMA formulation can form a highly transparent hydrogel after photopolymerization. After adding MOF, the color of various GelMA/MOF formulations and their corresponding hydrogels turned to darker with increasing MOF concentration. The UV-vis absorbance spectra of GelMA, GelMA/MOF formulations and photoinitiator (PI) solution (0.75%, w/v) were measured. As exhibited in Fig. 2b, the introduction of MOF leads to enhanced light absorption at 385 nm, meaning a competition for light absorption between MOF and PI, which would affect the photopolymerization of GelMA during the printing process. This competition could be useful for DLP to improve the printing precision and to prevent undesired curing out of the exposed areas [41]. To testify this, the GelMA and various GelMA/MOF formulations were printed using two STL models: one featuring a cube with vertical cylindrical holes and the other with horizontal cylindrical holes. As depicted in Fig. S2a, the GelMA ink encounters challenges in forming the desired hole inside the cube due to excessive photopolymerization. In contrast, Fig. S2b demonstrates that the internal hole structure appears to be more easily printed after incorporating the MOF. This phenomenon indicates that adding a moderate amount of MOF can enhance printing accuracy, enabling the creation of 3D objects with more complex structures.

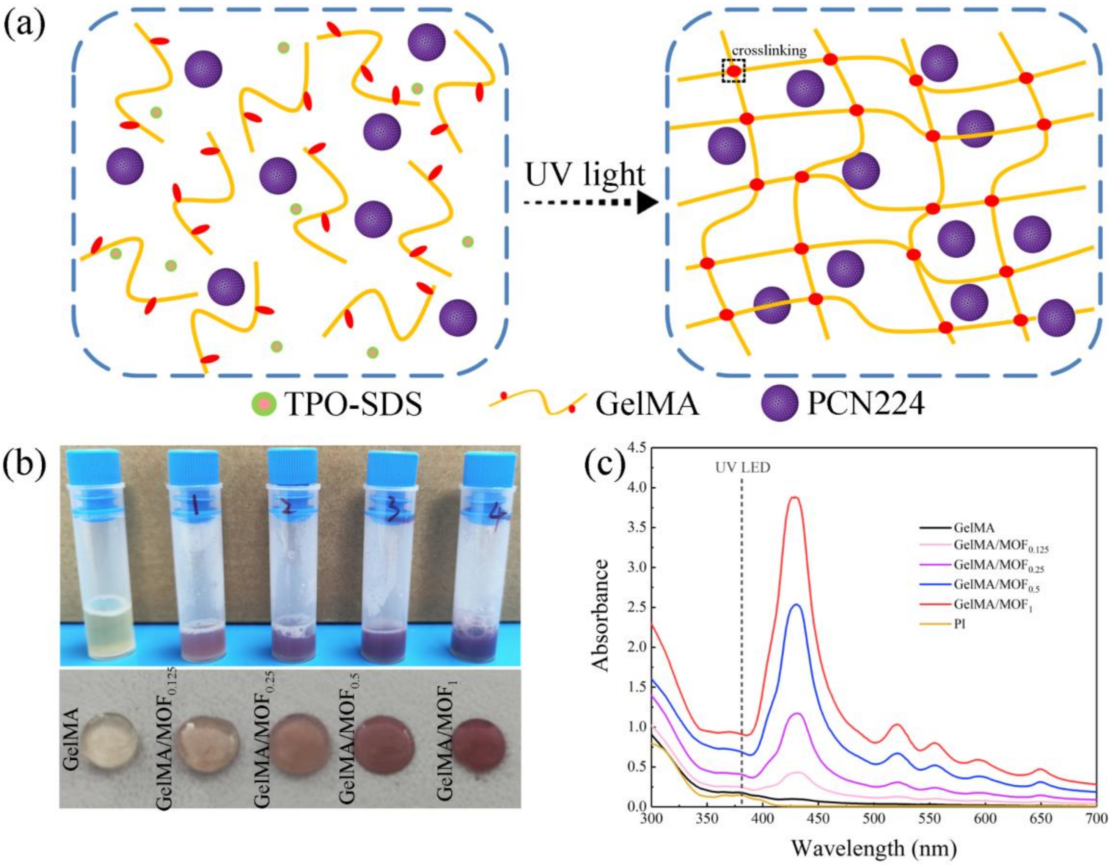

Fig. 2. (a) Schematic illustration of the cross-linked network of GelMA/MOF hydrogel. (b) Photographs of various formulations and corresponding hydrogels. (c) UV-vis absorbance spectra of GelMA formulation, GelMA/MOF formulations and PI

solution (0.75%, w/v).

Considering the effect of different MOF concentrations on photopolymerization, additional investigations were further conducted to determine the DLP printing parameters, specifically photorheology and curing behavior tests. As shown in Fig. 3a, all the formulations show rapid increase of G’ modulus, indicating that gels are formed in relatively short periods upon UV irradiation. This is a first indication of their suitability for DLP 3D printing, in principle. However, the presence of MOF induced variations in the photopolymerization kinetics of GelMA matrix. The start of curing reaction of the GelMA/MOF formulations was gradually delayed as the MOF concentrations increased (Fig. 3b), witnessed by an increased latency time (up to 13 s for GelMA/MOF$_1$). Meanwhile, also, the final storage modulus of the cured hydrogels decreases, indicating less cross-linked networks. These phenomena can be ascribed to the competition of UV light between MOF and PI, which decreases the rate of photoinitiation and thus the final conversion of acrylic double bonds [41]. To further determine the parameters for printing process, the curing behavior of GelMA and GelMA/MOF formulations were tested. As shown in Fig. S3a, these curves describe the relationships between the light intensity and curing thickness of the formulations. In addition, the relationships between the exposure time and the curing thickness are also tested (Fig. S3b). As expected, the curing thickness and the exposure time are linearly correlated at a constant light intensity [54]. These results are important for establishing optimal parameters in practical printing.

After optimizing the printing parameters, the fabrication of the GelMA/MOF hydrogels was conducted. Fig. 3c illustrates the fabrication process using the DLP printer. This equipment is based on the localized irradiation of pixels, following a digital model file, which enables the fabrication of a single layer of one object. Then, the solidified layer was moved upward, allowing the bottom of the vat to be covered with a new layer of uncured resins, and consequently allowing to perform this process over and over, until obtaining the desired 3D object [55]. In this case, once the curing behavior was determined, the GelMA/MOF hydrogels with complex 3D structures could be printed, obtaining objects with well-defined edges and holes, also in z direction. It must be noted that such complexity is not trivial for formulations which contain more than 80% of water, and the definition here obtained is in good agreement with the results obtained in vat photopolymerization for formulations with similar GelMA content [56]. Fig. S4 demonstrates the high model fidelity achieved by DLP 3D printing, with errors of the object measured basically within 0.1 mm. In addition, Fig. 3d exhibits the various shapes of GelMA/MOF hydrogels printed according to different wound defects, implying the potential to flexibly manufacture hydrogels matching the wound defect using DLP technology, thereby enabling personalized wound management.

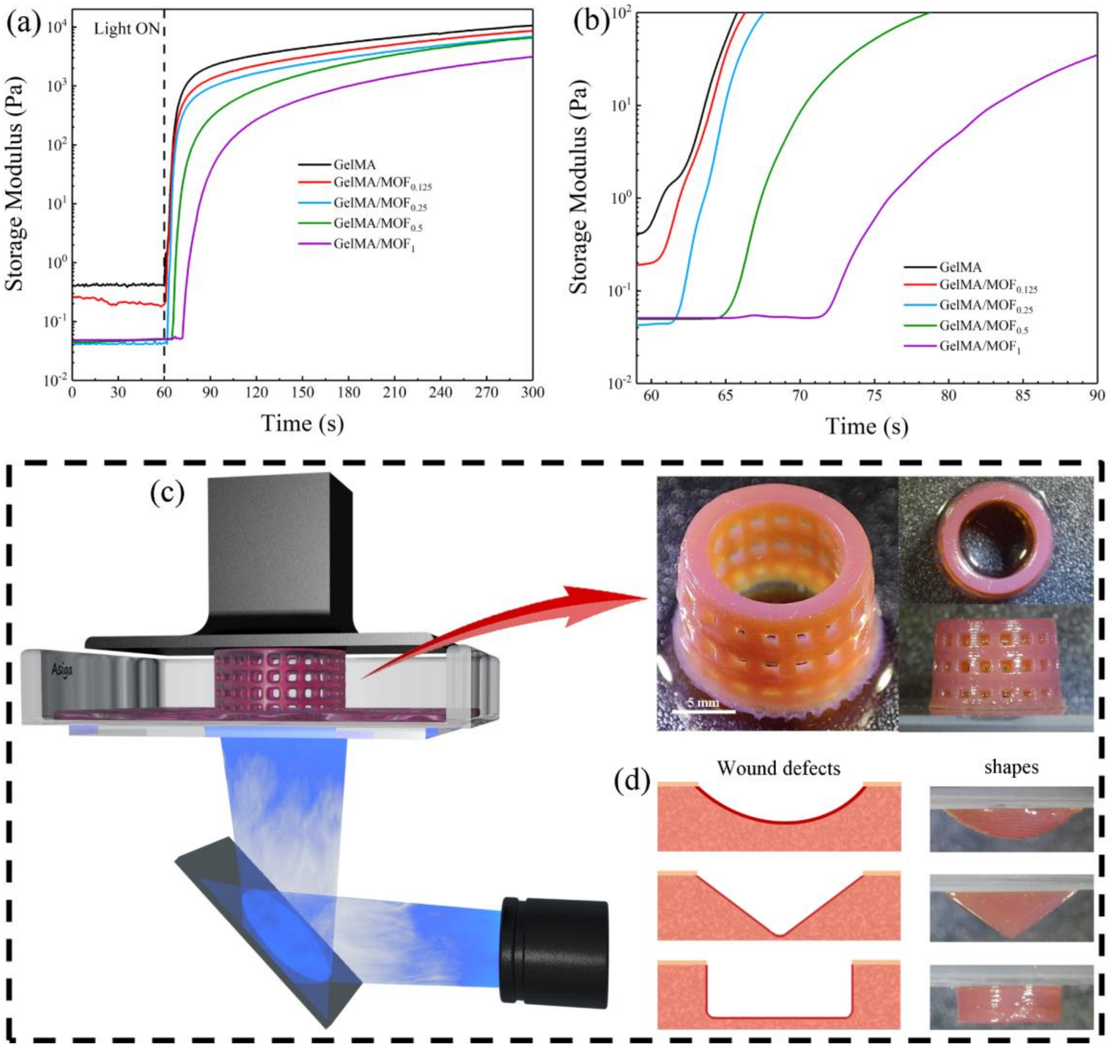

Fig. 3. (a) Photorheological curves of GelMA and GelMA/MOF formulations. (b) Photopolymerization kinetics of GelMA and GelMA/MOF formulations within 30 s of UV irradiation. (c) Schematic illustration of the printing process and the corresponding product. (d) Various shapes of wound defect models and their corresponding printed GelMA/MOF hydrogels.

3.3. Characterization of 3D-printed GelMA/MOF hydrogels

The micro-structure of the 3D-printed hydrogels were observed by FESEM after freeze-drying. Fig. 4a and b show that the morphology of lyophilized 3D-printed

GelMA and GelMA/MOF$_1$ hydrogels contain highly anisotropic networks and typical microporous structure, consistent with a cross-linked internal structure and suggesting large liquid absorption capacity. In comparation of the magnified images of Fig. 4a and b, the GelMA shows a relatively smooth surface, while GelMA/MOF$_1$ shows a rougher surface, which can be attributed to the presence of the insoluble granular MOF in GelMA matrix. The effect of the higher content of MOF are here showed, but similarly the GelMA/MOF$_{0.125}$, GelMA/MOF$_{0.25}$, and GelMA/MOF$_{0.5}$ specimens display the cross-linked and microporous structure, as reported in Fig. S5 in Supporting Information file. Therefore, it can be inferred that the MOF (as the filler) plays a role during curing, but once optimized printing parameters exerts little influence on the micro-structure of photopolymerized GelMA matrix, owing to the precise control offered by DLP technology for photopolymerization.

The mechanical properties of the 3D-printed GelMA/MOF hydrogels were assessed by DMA at 25 °C and 37 °C. As shown in Fig. 5a and b, the storage modulus of GelMA-based hydrogel initially increases and then decreases with the increasing concentration of MOF in the system. The probable cause of this phenomenon lies in that at lower concentrations of MOF ($c \leq 0.25$ mg/mL), the carboxyl groups within GelMA chains can coordinate with Zr_6 metal clusters present in MOF to form a more densely packed hydrogel structure [57, 58]. However, as the concentration of MOF continues to increase, their presence affects the photopolymerization of the GelMA matrix because of the optical competition, leading to a decrease in the crosslinking density of the hydrogel, in good agreement with photorheology tests. In addition, from Fig. 5a and b, as expected the increase in temperature enhances the chains mobility, subsequently leading to a lower storage moduli [59].

The swelling behavior and water retention of the printed hydrogels were also investigated. The result of swelling ratios (Fig. 5c) indicates that all freeze-dried hydrogels absorbed water rapidly, within 8 h, and then remained stable (measurement up to 48 h), without being destroyed. Interestingly, the swelling ratio was slightly reduced after adding a lower content of MOF ($c \leq 0.25$ mg/mL). This decrease could be related to the higher crosslinking density of the nanofillers, which consequently limits network expansion during absorption [30]. On the other hand, when the MOF content is higher ($c \geq 0.5$ mg/mL), the swelling ratio increased, potentially attributed to the looser network previously mentioned. To carefully tailor the final property of the hydrogel, several factors must be considered. On the one hand, the presence of the embedded nanofillers may hinder the movements of macromolecular chains decreasing the free volume between the GelMA chains, and thus reducing swelling. On the other hand, the effect of light absorption and printing parameters may result in decrease of crosslinking density, modifying the swelling behavior of the composite hydrogels [30]. Thus, according to desired applications, a proper trade-off must be conducted regarding the printability, mechanical properties, and swellability of the hydrogels. Fig. 5d exhibits the water retention capacity of printed hydrogels. All hydrogels exhibited a similar pattern, losing moisture and reaching equilibrium within 8 h. In general, this is a drawback since hydrogels lose their flexibility drying. In view of extending the applicability of hydrogels, in our next project, we aim at improving the water retention performance of printed hydrogels. The degradation behavior of printed hydrogels was also tested. As shown in Fig. S6, all hydrogels display good degradability within 30 days. It is also evident that hydrogels with higher crosslinking density (GelMA, GelMA/MOF$_{0.125}$, and GelMA/MOF$_{0.25}$) exhibited lower degradability, whereas those with lower crosslinking density (GelMA/MOF$_{0.5}$ and GelMA/MOF$_{1}$) degraded more rapidly.

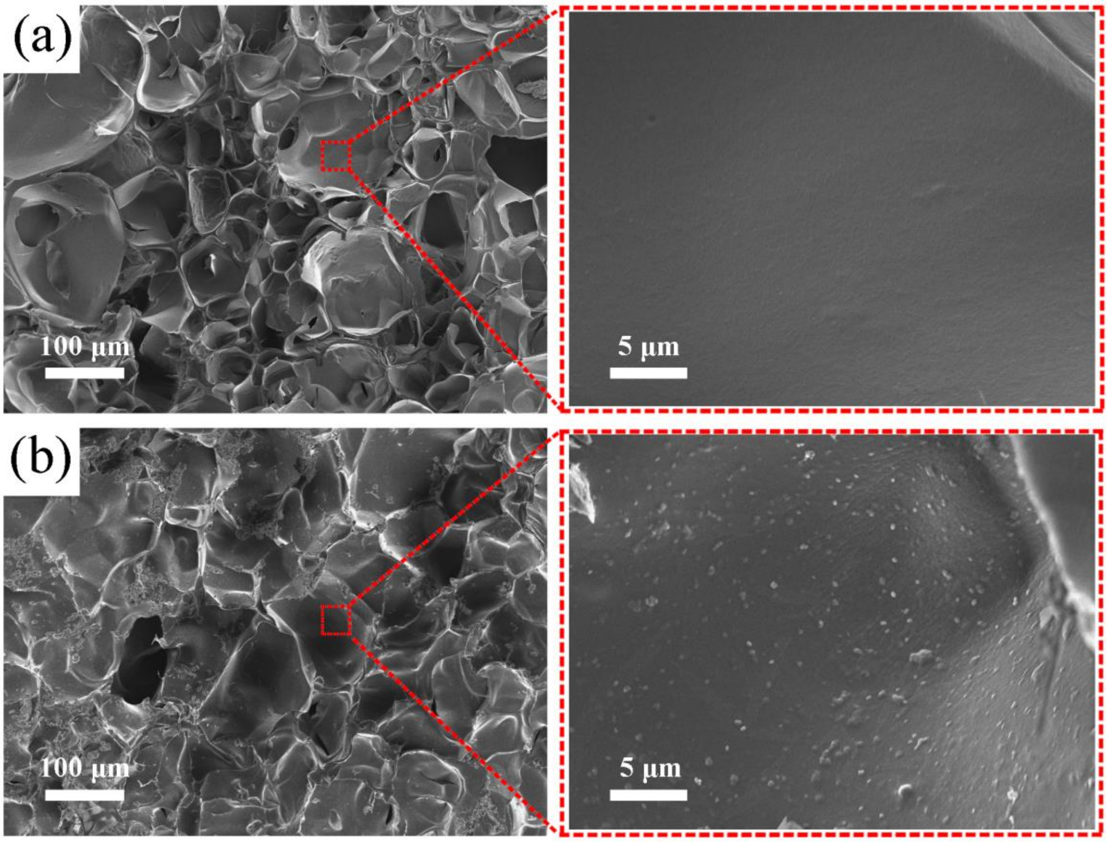

Fig. 4. Morphological structures of 3D-printed GelMA (a) and GelMA/MOF$_{1}$ hydrogels (b).

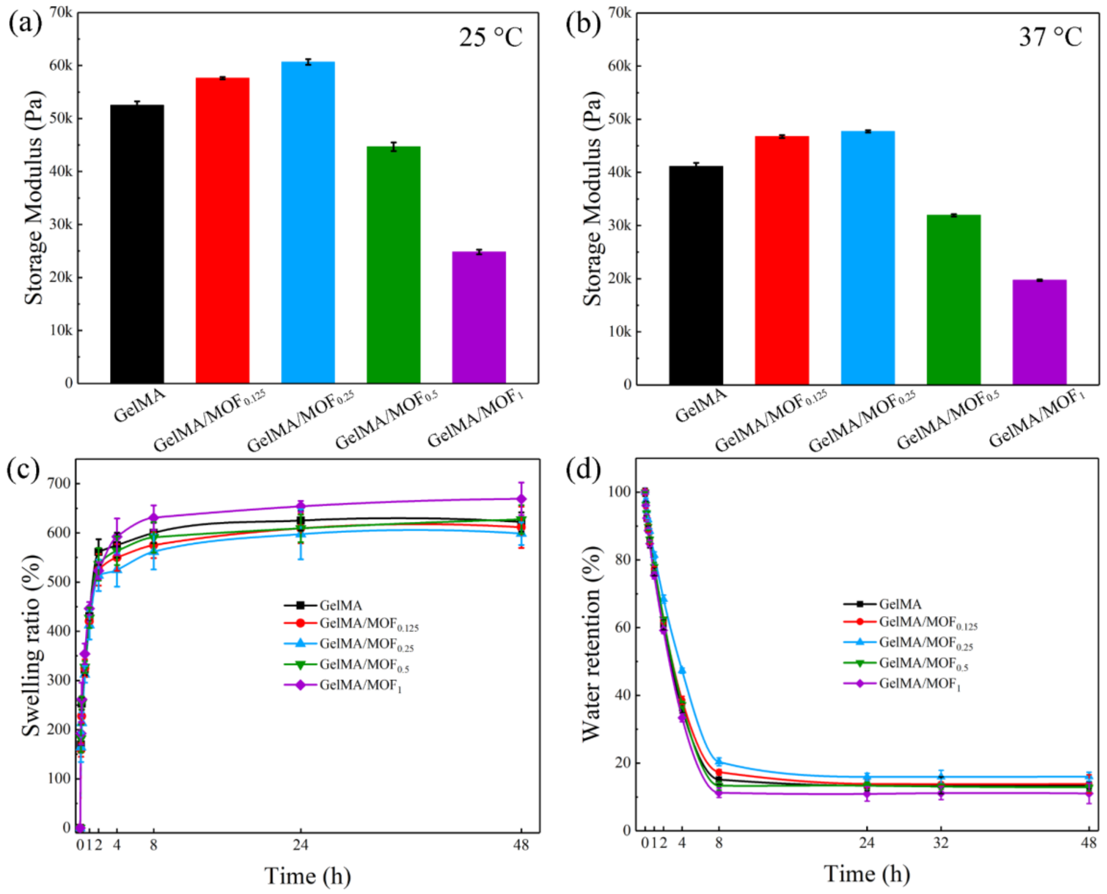

Fig. 5. (a-b) Storage modulus of 3D-printed GelMA and GelMA/MOF hydrogels at 25 °C and 37 °C, respectively. (c) Swelling ratio. (d) Water retention.

3.4. Photothermal and photodynamic performances of printed GelMA/MOF hydrogels

As a subclass of MOF materials, porphyrinic PCN-224 possesses excellent photothermal property and remarkable photodynamic activity [38, 53, 60]. Hence, the photothermal and photodynamic performances of the 3D-printed GelMA/MOF hydrogels were investigated. As shown in Fig. 6a to e, after exposure to visible light for 180 s, the hydrogels reached a temperature of 26.7 °C for GelMA, 32.3 °C for GelMA/MOF$_{0.125}$, 36.4 for GelMA/MOF$_{0.25}$, 40.0 °C for GelMA/MOF$_{0.5}$, and 41.2 °C for GelMA/MOF$_{1}$, respectively. Fig. 6f also displays the photothermal curves of these printed hydrogels within 180 s. Along with the increase in the amount of MOF incorporated, the photothermal capacity gradually enhanced in the order GelMA/MOF$_1$ > GelMA/MOF$_{0.5}$ > GelMA/MOF$_{0.25}$ > GelMA/MOF$_{0.125}$ > GelMA. Besides, it is worth noting that all the hydrogels exhibit a similar tendency, as the exposure time to light increases, the temperature remains around its maximum value. This phenomenon may be attributed to the evaporation of water within the hydrogel system, which limits the increase in temperature.

PCN-224 has already been demonstrated able to produce $^1O_2$ under light irradiation, which could be specifically trapped by DPBF, leading to a decrease in the absorbance at 415 nm [61]. Hence, DPBF was selected as the $^1O_2$ detector to compare the photodynamic activity of printed GelMA/MOF hydrogels. Fig. 6g to k display the UV-vis absorption spectra of DPBF co-incubated with these hydrogels after 5 min irradiation. As predicted, the GelMA/MOF$_1$ hydrogel caused the most significant decrease of absorption at 415 nm, indicating that this material could produce the largest amount of $^1O_2$, followed by GelMA/MOF$_{0.5}$, GelMA/MOF$_{0.25}$, GelMA/MOF$_{0.125}$, and GelMA. Similarly, the corresponding fitting curves (Fig. 6l) depicting the absorption decrease over time (at 415 nm) further suggest that the GelMA/MOF$_1$ achieved the highest efficiency in $^1O_2$ yield, followed by GelMA/MOF$_{0.5}$, GelMA/MOF$_{0.25}$, GelMA/MOF$_{0.125}$, and GelMA. Apparently, in this case, the GelMA hydrogel (without MOF) showed no reduction in DPBF absorbance under light irradiation for 5 min, confirming that the generation of $^1O_2$ is attributed to the presence of the MOF. To exclude time-degradation effects, the absorption spectra of DPBF co-incubated with GelMA/MOF$_1$ hydrogel in dark condition were recorded and reported in Fig. S7a. The absorbance at 415 nm remains stable after 5 min co-incubation, confirming that the degradation can be related only by the generation of $^1O_2$ in MOF, activated by light irradiation. Furthermore, to investigate the possible release of the MOF crystals from the network, the printed hydrogels were sonicated in PBS at 37 °C for 1 h, and the leakage was then detected collecting UV-vis spectra. As shown in Fig. S7b, no characteristic absorption peaks of MOF were observed in any group after 1 hour of sonication. The inset of the same figure also showed that all hydrogels were not damaged during the swelling, while the supernatant remained clear and transparent. Thus, it could be inferred that the MOF crystals are effectively embedded in GelMA matrix, even after swelling. In order to test the stability of photodynamic activity, $^1O_2$ detection was repeated after 30 min of exposure to visible light (~30 mW/cm^2) on these GelMA/MOF hydrogels, as shown by the fitting curves of $^1O_2$ yield in Fig. S8. All the GelMA/MOF hydrogels still exhibited photodynamic activity consistent with previous findings, although their $^1O_2$ generation efficiency slightly decreased, while obviously GelMA didn't show any activity. This demonstrates that the embedded MOFs maintain stable and repeatable $^1O_2$ generation [62, 63]. To check whether the radical generation modifies the polymeric networks, DMA tests were repeated on these light-exposed hydrogels. As shown in Fig. S9, the storage moduli of all hydrogels at 37 °C increased compared to pre-exposure values, with more significant increases observed in hydrogels which contain higher amount of MOF. This is can be related to a water loss caused by light exposure, as the storage modulus typically has a negative correlation with the water content of hydrogels [64]. On the other hand, it is not possible to exclude that the radicals' generation can also slightly modify the polymeric network, creating new cross-linking point which can be consistent with an increase of the moduli. To better evaluate this aspect specifical ageing tests should be performed, which are beyond the scope of this manuscript and will be better investigated in future activities.

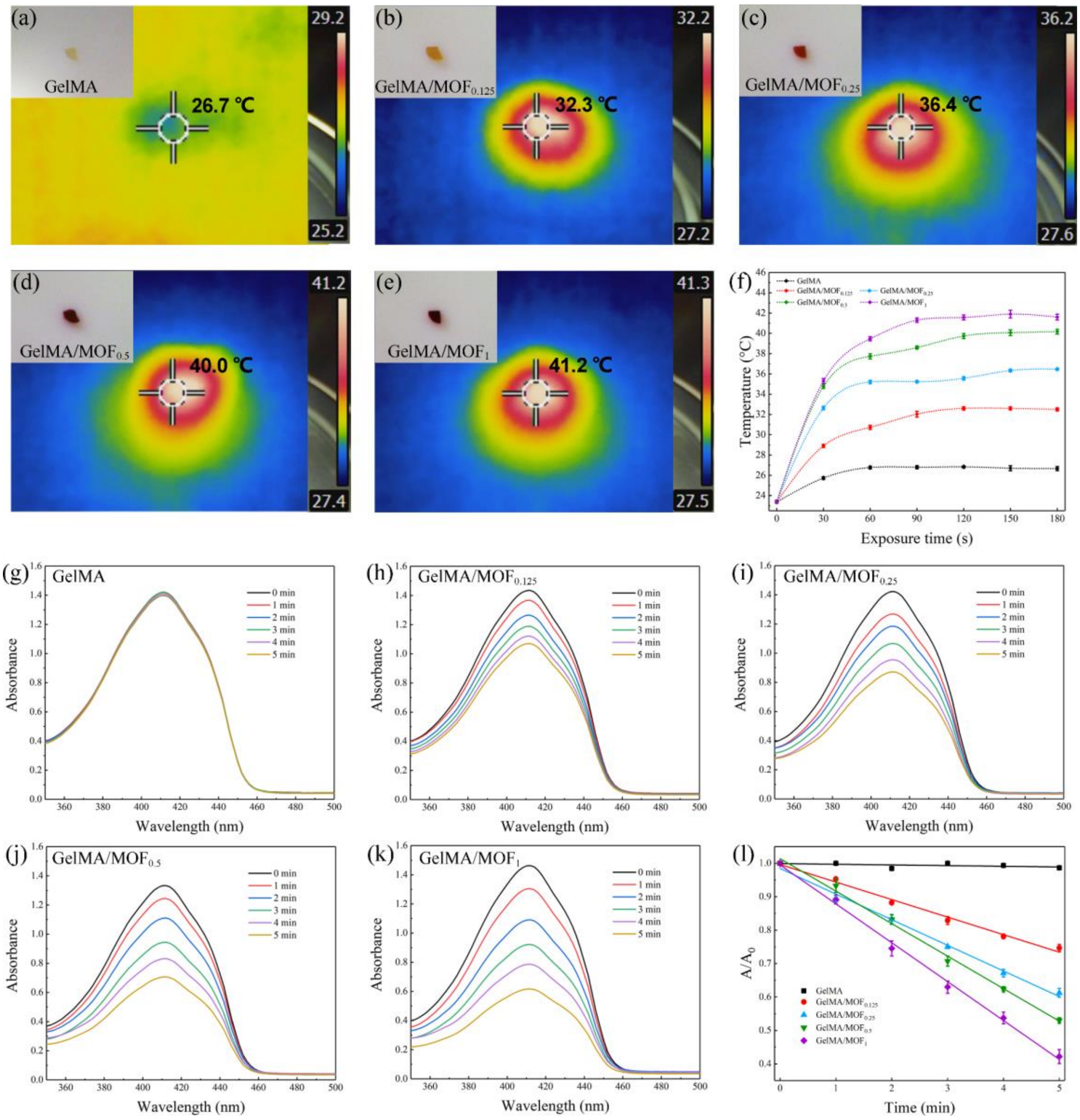

Fig. 6. (a-e) Digital images and surface thermal under visible illumination (~30 mW/cm^2) for 180 s. (f) Temperature rise curves. (g-k) UV-vis spectra of DPBF under

illumination (520 nm) in presence of GelMA and GelMA/MOF hydrogels. (l) Linear fitting of $^1O_2$ yields.

3.5. Antibacterial efficacy

Based on the above results, it was natural thinking that after incorporating a greater amount of MOF into the GelMA hydrogel, the photothermal and photodynamic abilities could be enhanced simultaneously. Herein, two common strains (*S. aureus* and *E. coli*), which are responsible for most wound infections, were used to evaluate the antibacterial performance of the printed GelMA/MOF hydrogels [65]. The bacterial suspensions without contacting printed hydrogels were set as blank groups. Fig. S10a and b displayed the surviving bacterial colonies of *S. aureus* and *E. coli* on LB agar plates, respectively. In comparison to the blank groups (dark and light), a minimal decrease in bacterial survival could be observed after the bacterial suspensions were exposed to the light illumination alone, indicating that the light caused almost no damage to the bacteria. In the dark groups, both *S. aureus* and *E. coli* grew quite well after contacting with GelMA and GelMA/MOF hydrogels for 30 min. However, under light illumination, the viable colonies of both types of bacteria decreased as the MOF content increased in the GelMA/MOF hydrogels. This phenomenon demonstrates that GelMA/MOF hydrogels could effectively eliminate bacteria upon light irradiation, and the antibacterial efficiency increases together with the MOF content. The quantified antibacterial efficiencies against *S. aureus* and *E. coli* were displayed in Fig. 7a and b, respectively. The light alone caused a 27.29%

reduction against *S. aureus* and a 26.35% reduction against *E. coli*, which could be considered negligible in terms of bactericidal effect [38]. Additionally, all the dark groups displayed slight reduction against *S. aureus* and *E. coli*, which could be attributed to the bacterial adhesion on GelMA or GelMA/MOF hydrogels, rather than a bactericidal action. After the hydrogels were illuminated under light, GelMA/MOF$_1$ hydrogel exhibited the highest antibacterial efficiency against *S. aureus* (> 99.99%) and *E. coli* (> 99.99%), followed by GelMA/MOF$_{0.5}$ (*S. aureus*: 99.94%, *E. coli*: 99.65%), GelMA/MOF$_{0.25}$ (*S. aureus*: 99.42%, *E. coli*: 95.43%), GelMA/MOF$_{0.125}$ (*S. aureus*: 90.85%, *E. coli*: 62.54%), and GelMA (*S. aureus*: 21.67%, *E. coli*: 21.90%). Here, the slight reduction observed in GelMA hydrogels against both *S. aureus* and *E. coli* also could be attributed to bacterial adhesion rather than sterilization. The results of the antibacterial tests are consistent with the findings of the photothermal/photodynamic analysis.

SEM was also employed to observe the morphologies of bacteria after treatment with GelMA/MOF hydrogels. Herein, bacteria were inoculated on GelMA and GelMA/MOF$_x$ hydrogels and illuminated for 30 min for comparison. As shown in Fig. 7c, *S. aureus* exhibited typical morphologies with intact spherical shapes and smooth surfaces on GelMA hydrogel. However, on GelMA/MOF$_1$ hydrogel, the membranes of *S. aureus* were severely deformed and ruptured (red arrows). The same phenomenon could be observed in Fig. 7b, where *E. coli* maintained their typical and intact rod shapes on GelMA hydrogel, while appearing wrinkled and ruptured on GelMA/MOF$_1$ hydrogel (red arrows). Additionally, the bacteria treated with

GelMA/MOF$_{0.125}$, GelMA/MOF$_{0.25}$, and GelMA/MOF$_{0.5}$ hydrogels are shown in Fig. S11. The morphological deformation of *S. aureus* and *E. coli* is also observed, with the degree becoming more pronounced as the MOF content increases. Thus, the bactericidal action of the GelMA/MOF hydrogels could be ascribed to a synergism of MOF-triggered photothermal and photodynamic processes. This combined effect can disrupt the structure of the bacterial membrane, leading to the outflow of intracellular substances and ultimately triggering apoptosis [66, 67].

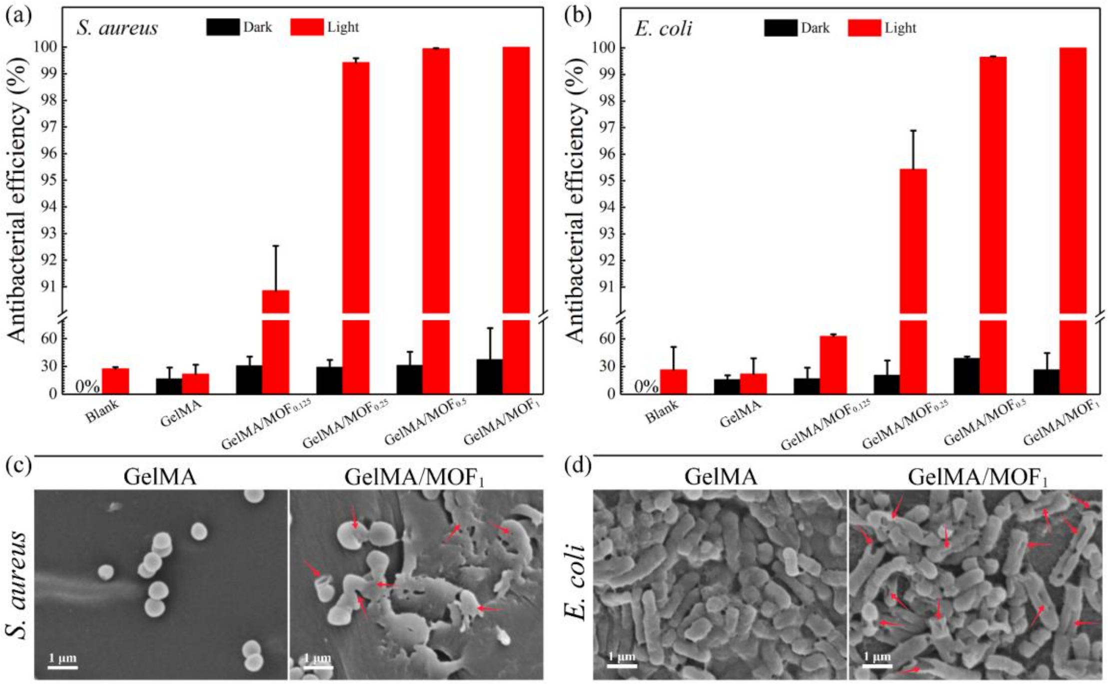

Fig. 7. Antibacterial efffciencies of GelMA and GelMA/MOF hydrogels against *S. aureus* (a) and *E. coli* (b). SEM images of *S. aureus* (c) and *E. coli* (d) contacted with GelMA and GelMA/MOF$_1$ under visible light for 30 min irradiation.

3.6. Hemocompatibility and cytocompatibility

An ideal medical dressing should be biocompatible with both blood cells and skin tissue cells [68]. Here, *in vitro* hemolysis and cytotoxicity assays were conducted to evaluate the biocompatibilities of printed GelMA/MOF hydrogels. As depicted in Fig. 8a, the hemolysis ratios of GelMA and GelMA/MOF hydrogels remained below the specified limit (5% hemolysis) after 3-hour co-incubation, indicating their good compatibility with blood cells [69]. The inset in Fig. 8a illustrates the supernatants of each group, where RBCs ruptured after incubation in DI water (positive control), leading to a bright red in the supernatant. Conversely, the RBCs co-incubated with GelMA and GelMA/MOF hydrogel exhibited supernatants that appeared nearly colorless and transparent, like the incubation in PBS (negative), indicating insignificant levels of hemolysis. Fig. 8b displays the cytocompatibility of printed GelMA and GelMA/MOF hydrogels. After a 48 h co-culture with L929 cells, the cell viability in all sample groups exceeded 80%, confirming the low cytotoxicity of these GelMA/MOF hydrogels [70]. The Live/Dead staining assay was also performed to assess the condition of L929 cells following the cytotoxicity test. As shown in Fig. 8c, the majority of spindle-shaped cells exhibited green fluorescence in negative control and all hydrogel groups, corresponding to the living cells. Few dead cells, characterized by red fluorescence and a globular shape, were observed in these groups, suggesting negligible cytotoxicity. The results of *in vitro* hemolysis and cytotoxicity assays demonstrate the favorable biocompatibility of printed GelMA/MOF hydrogels, positioning them as promising candidates for use in wound dressings.

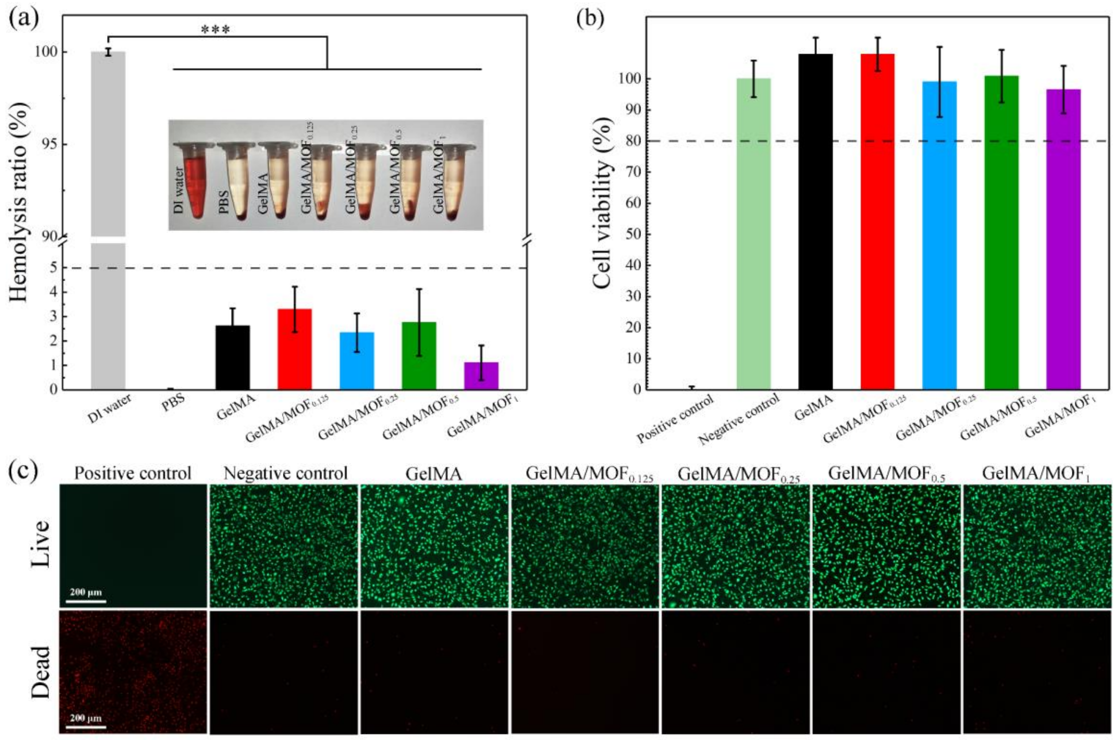

Fig. 8. (a) Hemolysis assay. (b) Cell viability of cytotoxicity assay. (c) Live/Dead staining assay. (*** represents $P < 0.001$).

4. Conclusions

In summary, this work reports the fabrication of printable MOF-based nanocomposite hydrogels through DLP 3D printing, utilizing photocurable GelMA resins and incorporating PCN-224 as a nanofiller. During the printing, higher UV-light intensity and longer slicing time were required due to the photo-competitive effect of the MOF, while the printing precision could be improved. This facilitates the construction of more intricate and fidelity hydrogel structures tailored to clinical wound defects. Moreover, the incorporation of MOF imparts photothermal and photodynamic properties to the printed hydrogels, with both effects amplifying as MOF concentration increases. However, a high concentration of MOF affects printing and the mechanical properties of the nanocomposite hydrogels. The result of antibacterial assay revealed an enhancement in antibacterial performance with increasing MOF concentration, with GelMA/MOF$_1$ exhibiting the highest antibacterial efficiency against *S. aureus* (> 99.99%) and *E. coli* (> 99.99%) for 30 min illumination, followed by GelMA/MOF$_{0.5}$ (*S. aureus*: 99.94%, *E. coli*: 99.65%), GelMA/MOF$_{0.25}$ (*S. aureus*: 99.42%, *E. coli*: 95.43%), and GelMA/MOF$_{0.125}$ (*S. aureus*: 90.85%, *E. coli*: 62.54%). Additionally, all printed GelMA/MOF hydrogels demonstrated excellent cytocompatibility and hemocompatibility. Therefore, utilizing MOF as a functional filler in the preparation of biocompatible photodynamic/photothermal hydrogels through DLP 3D printing not only mitigates the risks associated with MOF drug residue but also allows for the customization of wound dressings matching specific skin defects. In the next future, this additive approach will hold significant clinical relevance in light therapy.

Declaration of competing interest

The authors declare no competing financial interest.

Supporting Information

Preliminary 3D printing experiments 3D printed parts with increasing content of MOFs, 3D printing working curves, evaluation of 3D printing fidelity, additional SEM experiments on freeze-dried matrices, degradation test, leakage test, evaluation of $^1O_2$ yields after ageing, DMA measurements after UV ageing, additional bacterial test and additional SEM images of bacteria are supplied as Supporting Information.

Acknowledgments

This work is supported by the funds of China Scholarship Council (No. 202206790041).

Under the National Plan for Complementary Investments to the NRRP, project "D34H—Digital Driven Diagnostics, prognostics and therapeutics for sustainable Health care" (project code: PNC0000001), Spoke 4 funded by the Italian Ministry of University and Research.

References

(1) Dong, R.; Guo, B. Smart Wound Dressings for Wound Healing Nano Today 2021,41, 101290.

(2) Chang, R.Y.K.; Nang, S.C.; Chan, H.-K.; Li J. Novel Antimicrobial Agents for Combating Antibiotic-Resistant Bacteria Adv. Drug Deliv. Rev. 2022, 187, 114378.

(3) Nie, X.; Wu, S.; Mensah, A.; Wang Q.; Huang, F.; Wei, Q. FRET as a Novel Strategy to Enhance the Singlet Oxygen Generation of Porphyrinic MOF Decorated Self-Disinfecting Fabrics Chem. Eng. J. 2020, 395, 125012.

(4) Zhou, C.; Wang, Q.; Jiang, J.; Gao, L. Nanozybiotics: Nanozyme-Based Antibacterials Against Bacterial Resistance Antibiotics 2022, 11, 390.

(5) Liu, S.; Wang, B.; Yu, Y.; Liu, Y.; Zhuang, Z.; Zhao, Z.; Feng, G.; Qin, A.; Tang, B.Z. Cationization-Enhanced Type I and Type II ROS Generation for Photodynamic Treatment of Drug-Resistant Bacteria ACS Nano 2022, 16, 9130-9141.

(6) Liu, C.; Chang, Q.; Fan, X.; Meng, N.; Lu, J.; Shu, Q.; Xie, Y.; Celia, C.; Wei, G.; Deng, X. Rational Construction of CQDs-Based Targeted Multifunctional Nanoplatform for Synergistic Chemo-Photothermal Tumor Therapy J. Colloid Interf. Sci. 2024, 677, 79-90.

(7) Zhao, M.; Yang, H.; Sun, Z.; Li, Y.; Hou, L.; Zhang, S.; Jin, L.; Shen, B.; Xia, B. MoS_2 Nanocomposites Loaded with Zinc Phthalocyanine for NIR Light-Triggered Photothermal/Photodynamic Therapy of Breast Cancer ACS Appl. Nano Mater. 2024, 7, 16372-16384.

(8) Jiang, X.; Huang, Z.; Liu, Z.; Wang, S.; Qiu, Y.; Su, X.; Wang, Y.; Xu, H.; MOF-Derived Oxygen-Deficient Titania-Mediated Photodynamic/Photothermal-Enhanced Immunotherapy for Tumor Treatment ACS Appl. Mater. Interfaces 2024, 16, 34591-34606.

(9) Han, X.; Boix, G.; Balcerzak, M.; Moriones, O.H.; Cano‐Sarabia, M.; Cortés, P.; Bastús, N.; Puntes, V.; Llagostera, M.; Imaz, I. Antibacterial Films Based On MOF Composites That Release Iodine Passively Or Upon Triggering By Near‐Infrared Light Adv. Funct. Mater. 2022, 32, 2112902.

(10) Li, S.-Y.; Cheng, H.; Qiu, W.-X.; Zhang, L.; Wan, S.-S.; Zeng, J.-Y.; Zhang, X.-Z. Cancer Cell Membrane-Coated Biomimetic Platform For Tumor Targeted Photodynamic Therapy And Hypoxia-Amplified Bioreductive Therapy Biomaterials 2017, 142 149-161.

(11) Chao, D.; Dong, Q.; Yu, Z.; Qi, D.; Li, M.; Xu, L.; Liu, L.; Fang, Y.; Dong, S. Specific Nanodrug for Diabetic Chronic Wounds Based on Antioxidase-Mimicking MOF-818 Nanozymes J. Am. Chem. Soc. 2022, 144, 23438-23447.

(12) Chansi; Upreti, S.; Punya; Singh, J.; Ghosh, M.P.; Basu, T. Rapid Electrochemical Quantification for In Vitro Release Trait of Ophthalmic Drug Loaded within Mucoadhesive Metal Organic Framework (MOF) Chem. Select 2021, 6, 3006-3012.

(13) Li, J.; Song, S.; Meng, J.; Tan, L.; Liu, X.; Zheng, Y.; Li, Z.; Yeung, K.W.K.; Cui, Z.; Liang, Y. 2D MOF Periodontitis Photodynamic Ion Therapy J. Am. Chem. Soc. 2021, 143, 15427-15439.

(14) Gwon, K.; Han, I.; Lee, S.; Kim, Y.; Lee, D.N. Novel Metal–Organic Framework-Based Photocrosslinked Hydrogel System for Efficient Antibacterial Applications ACS Appl. Mater. Interfaces2020, 12, 20234-20242.

(15) Huang, K.; Liu, W.; Wei, W.; Zhao, Y.; Zhuang, P.; Wang, X.; Wang, Y.; Hu, Y.; Dai, H. Photothermal Hydrogel Encapsulating Intelligently Bacteria-Capturing Bio-MOF for Infectious Wound Healing ACS Nano 2022, 16, 19491-19508.

(16) Wang, Z.; Liang, X.; Wang, G.; Wang, X.; Chen, Y. Emerging Bioprinting for Wound Healing Adv. Mater. 2023, 2304738.

(17) Farahani, M.; Shafiee, A. Wound Healing: from Passive to Smart Dressings Adv. Healthc. Mater. 2021, 10, 2100477.

(18) Zhang, M.; Zhao, X. Alginate Hydrogel Dressings for Advanced Wound Management Int. J. Biol. Macromol. 2020, 162, 1414-1428.

(19) Salas, A.; Zanatta, M.; Sans, V.; Roppolo, I. Chemistry in Light-Induced 3D Printing Chemtexts 2023, 9, 4.

(20) Mogli, G.; Reina, M.; Chiappone, A.; Lamberti, A.; Pirri, C.F.; Roppolo, I.; Stassi, S. Self-Powered Integrated Tactile Sensing System Based on Ultrastretchable, Self-Healing and 3D Printable Ionic Conductive Hydrogel Adv. Funct. Mater. 2024, 34, 2307133.

(21) Hu, Y.; Tang, H.; Xu, N.; Kang, X.; Wu, W.; Shen, C.; Lin, J.; Bao, Y.; Jiang, X.; Luo Z. Adhesive, Flexible, and Fast Degradable 3D-Printed Wound Dressings with a Simple Composition Adv. Healthc. Mater. 2024, 13, 2302063.

(22) Deng, S.; Wu, J.; Dickey, M.D.; Zhao, Q.; Xie, T. Rapid Open-Air Digital Light 3D Printing of Thermoplastic Polymer Adv. Mater. 2019,31, 1903970.

(23) He, X.-C.; Chen, X.-N.; Liu, Y.-H.; Zhong, X.; Qiang, L.; Wang, H.-Q.; Wang, F.-Z.; Wang, J.-S.; Li, C.-H.; Zheng, P.-F. A Blue Light 3D Printable Hydrogel with Water Absorption, Antibacterial, and Hemostatic Properties for Skin Wound Healing Chem. Eng. J. 2024, 493, 152439.

(24) Tabriz, A.G.; Douroumis, D. Recent Advances in 3D Printing for Wound Healing: a Systematic Review J. Drug Deliv. Sci. Tec. 2022, 74, 103564.

(25) Caprioli, M.; Roppolo, I.; Chiappone, A.; Larush, L.; Pirri, C.F.; Magdassi, S. 3D-Printed Self-Healing Hydrogels via Digital Light Processing Nat. Commun. 2021, 12, 2462.

(26) Villata, S.; Canta, M.; Baruffaldi, D.; Pavan, A.; Chiappone, A.; Pirri, C.F.; Frascella, F.; Roppolo, I. 3D Printable Acrylate Polydimethylsiloxane Resins for Cell Culture and Drug Testing Biomater. Sci. 2023, 11, 2950-2959.

(27) Zanon, M.; Montalvillo-Jiménez, L.; Cue-López, R.; Martínez-Campos, E.; Sangermano, M.; Chiappone, A.; Bosch, P. Vat 3D Printing of Full-Alginate Hydrogels via Thiol-Ene Reactions towards Tissue Engineering Applications Polym. Chem. 2023, 14, 4856-4868.

(28) Gugulothu, S.B.; Chatterjee, K. Visible Light-Based 4D-Bioprinted Tissue Scaffold ACS Macro Lett. 2023, 12, 494-502.

(29) Mo, X.; Ouyang, L.; Xiong, Z.; Zhang, T. Advances in Digital Light Processing of Hydrogels Biomed. Mater. 2022,17, 042002.

(30) Cafiso, D.; Septevani, A.A.; Noè, C.; Schiller, T.; Pirri, C.F.; Roppolo, I.; Chiappone, A. 3D Printing of Fully Cellulose-Based Hydrogels by Digital Light Processing SM&T 2022, 32, E00444.

(31) Daly, A.C.; Critchley, S.E.; Rencsok, E.M.; Kelly, D.J. A Comparison of Different Bioinks for 3D

Bioprinting of Fibrocartilage and Hyaline Cartilage Biofabrication 2016, 8, 045002.

(32) Li, S.; Huang, C.; Liu, H.; Han, X.; Wang, Z.; Huang, J.; Yan, Y.; Wang, Z. A Silk Fibroin Methacryloyl-Modified Hydrogel Promoting Cell Adhesion for Customized 3D Cell-Laden Structures ACS. Appl. Polym. Mater. 2022, 4, 7014-7024.

(33) Villata, S.; Canta, M.; Baruffaldi, D.; Roppolo, I.; Pirri, C.F.; Frascella, F. 3D Bioprinted Gelma Platform for the Production of Lung Tumor Spheroids; Bioprinting 2023, 36, E00310.

(34) Jing, X.; Xu, C.; Su, W.; Ding, Q.; Ye, B.; Su, Y.; Yu, K.; Zeng, L.; Yang, X.; Qu, Y. Photosensitive and Conductive Hydrogel Induced Innerved Bone Regeneration for Infected Bone Defect Repair Adv. Healthc. Mater. 202312, 2201349.

(35) Song, P.; Li, M.; Zhang, B.; Gui, X.; Han, Y.; Wang, L.; Zhou, W.; Guo, L.; Zhang, Z.; Li, Z. DLP Fabricating of Precision Gelma/HAP Porous Composite Scaffold for Bone Tissue Engineering Application Compos. B. Eng. 2022, 244, 110163.

(36) Li, W.; Hu, X.; Liu, H.; Tian, J.; Li, L.; Luo, B.; Zhou, C.; Lu, L. 3D Light-Curing Printing to Construct Versatile Octopus-Bionic Patches J. Mater. Chem. B 2023, 11, 5010-5020.

(37) Shen, J.; Song, W.; Liu, J.; Peng, X.; Tan, Z.; Xu, Y.; Liu, S.; Ren, L. 3D Bioprinting by Reinforced Bioink Based on Photocurable Interpenetrating Networks for Cartilage Tissue Engineering; International J. Biol. Macromol. 2024,254, 127671.

(38) Han, D.L.; Han, Y.J.; Li, J.; Liu, X.M.; Yeung, K.W.K.; Zheng, Y.F.; Cui, Z.D.; Yang, X.J.; Liang, Y.Q.; Li, Z.Y.; Zhu, S.L.; Yuan, X.B.; Feng, X.B.; Yang, C.; Wu, S.L. Enhanced Photocatalytic Activity and Photothermal Effects of Cu-Doped Metal-Organic Frameworks for Rapid Treatment of Bacteria-Infected Wounds Appl. Catal. B-Environ. 2020, 261, 118248.

(39) Cao, Y.; Zhang, S.; Lv, Z.; Yin, N.; Zhang, H.; Song, P.; Zhang, T.; Chen, Y.; Xu, H.; Wang, Y. An Intelligent Nanoplatform for Orthotopic Glioblastoma Therapy by Nonferrous Ferroptosis Adv. Funct. Mater. 2022, 32, 2209227.

(40) Zhu, Z.; Wang, L.; Peng, Y.; Chu, X.; Zhou, L.; Jin, Y.; Guo, H.; Gao, Q.; Yang, J.; Wang, X. Continuous Self-Oxygenated Double-Layered Hydrogel under Natural Light for Real-Time Infection Monitoring; Enhanced Photodynamic Therapy, and Hypoxia Relief in Refractory Diabetic Wounds Healing Adv. Funct. Mater. 2022, 32, 2201875.

(41) Gastaldi, M.; Cardano, F.; Zanetti, M.; Viscardi, G.; Barolo, C.; Bordiga, S.; Magdassi, S.; Fin, A.; Roppolo, I. Functional Dyes in Polymeric 3D Printing: Applications and Perspectives ACS Materials Lett. 2020, 3, 1-17.

(42) Jain, T.; Baker, H.B.; Gipsov, A.; Fisher, J.P.; Joy, A.; Kaplan, D.S.; Isayeva, I. Impact of Cell Density on the Bioprinting of Gelatin Methacrylate (Gelma) Bioinks Bioprinting 2021, 22, E00131.

(43) Schuurman, W.; Levett, P.A.; Pot, M.W.; Van Weeren, P.R.; Dhert, W.J.; Hutmacher, D.W.; Melchels, F.P.; Klein, T.J.; Malda, J. Gelatin-Methacrylamide Hydrogels as Potential Biomaterials for Fabrication of Tissue-Engineered Cartilage Constructs Macromol. Biosci. 2013, 13, 551-561.

(44) Shirahama, H.; Lee, B.H.; Tan, L.P.; Cho, N.-J. Precise Tuning of Facile One-Pot Gelatin Methacryloyl (Gelma) Synthesis Sci. Rep. 2016, 6, 31036.

(45) Dai, W.; Zhang, L.; Yu, Y.; Yan, W.; Zhao, F.; Fan, Y.; Cao, C.; Cai, Q.; Hu, X.; Ao, Y. 3D Bioprinting of Heterogeneous Constructs Providing Tissue-Specific Microenvironment Based on Host-Guest Modulated Dynamic Hydrogel Bioink for Osteochondral Regeneration Adv. Funct. Mater. 2022, 32, 2200710.

(46) Zhu, T.; Jiang, C.; Wang, M.; Zhu, C.; Zhao, N.; Xu, J. Skin-Inspired Double-Hydrophobic-Coating Encapsulated Hydrogels with Enhanced Water Retention Capacity Adv. Funct. Mater. 2021, 31,

2102433.

(47) Sun, X.; Yang, J.; Ma, J.; Wang, T.; Zhao, X.; Zhu, D.; Jin, W.; Zhang, K.; Sun, X.; Shen, Y.; Three-Dimensional Bioprinted BMSCS-Laden Highly Adhesive Artificial Periosteum Containing Gelatin-Dopamine and Graphene Oxide Nanosheets Promoting Bone Defect Repair Biofabrication 2023, 15, 025010.

(48) Aldana, A.A.; Valente, F.; Dilley, R.; Doyle, B. Development of 3D Bioprinted Gelma-Alginate Hydrogels with Tunable Mechanical Properties Bioprinting 2021, 21, E00105.

(49) Wang, Y.; Ying, M.L.; Zhang, M.; Ren, X.H.; Kim, I.S. Development of Antibacterial and Hemostatic PCL/Zein/Zno-Quaternary Ammonium Salts Nps Composite Mats as Wound Dressings Macromol. Mater. Eng. 2021, 306, 2100587.

(50) Nie, X.L.; Wu, S.L.; Mensah, A.; Wang, Q.Q.; Huang, F.L.; Li, D.W.; Wei, Q.F. Insight into Light-Driven Antibacterial Cotton Fabrics Decorated by In Situ Growth Strategy J. Colloid Interf. Sci. 2020, 579, 233-242.

(51) Wang, Y.; Li, Z.; Liao, S.; Kong, Y.; Wang, Q.; Wei, Q. In Situ Biosynthetic BC/Zeolite Hybrid Hemostat for Quick Clot J. Appl. Polym. Sci. 2023, 140, E54315.

(52) Li, Y.; Chen, S.; Zhang, M.; Ma, X.; Zhao, J.; Ji, Y. Novel Injectable; Self-Healing; Long-Effective Bacteriostatic; and Healed-Promoting Hydrogel Wound Dressing and Controlled Drug Delivery Mechanisms ACS Appl. Mater. Interfaces 2024, 16, 2140-2153.

(53) Jin, P.X.; Wang, L.; Ma, X.L.; Lian, R.; Huang, J.W.; She, H.D.; Zhang, M.Y.; Wang, Q.Z. Construction of Hierarchical Znin$_{2}$s$_{4}$@PCN-224 Heterojunction for Boosting Photocatalytic Performance in Hydrogen Production and Degradation Oof Tetracycline Hydrochloride Appl. Catal. B-Environ. 2021, 284, 119762.

(54) Gastaldi, M.; Spiegel, C.A.; Vazquez-Martel, C.; Barolo, C.; Roppolo, I.; Blasco, E. 4D Printing of Light Activated Shape Memory Polymers with Organic Dyes Mol. Syst. Des. Eng. 2023,8, 323-329.

(55) Salas, A.; Pazniak, H.; Gonzalez-Julian, J.; Bianco, S.; Amici, J.; Ouisse, T.; Roppolo, I.; Cocuzza, M. Development of Polymeric/Mxenes Composites towards 3D Printable Electronics Compos. B. Eng. 2023, 263, 110854.

(56) Ye, W.; Li, H.; Yu, K.; Xie, C.; Wang, P.; Zheng, Y.; Zhang, P.; Xiu, J.; Yang, Y.; Zhang, F. 3D Printing of Gelatin Methacrylate-Based Nerve Guidance Conduits with Multiple Channels Mater. Des. 2020, 192, 108757.

(57) Shi, R.; Zhang, Z.; Yang, F.; Zhong, C. Simultaneously Anchoring Free Carboxyl and Sulfonate Groups into a Metal-Organic Framework for High Proton Conductivity Microporous Mesoporous Mater. 2022, 343, 112192.

(58) Xin, J.; Yang, Z.; Zhang, S.; Sun, L.; Wang, X.; Tang, Y.; Xiao, Y.; Huang, H.; Li, W. Fast Fabrication of "All-In-One" Injectable Hydrogels as Antibiotic Alternatives for Enhanced Bacterial Inhibition and Accelerating Wound Healing J. Nanobiotechnol. 2024, 221, 439.

(59) Janmaleki, M.; Liu, J.; Kamkar, M.; Azarmanesh, M.; Sundararaj, U.; Nezhad, A.S. Role of Temperature on Bio-Printability of Gelatin Methacryloyl Bioink in Two-Step Cross-Linking Strategy for Tissue Engineering Applications Biomed. Mater. 2020, 16, 015021.

(60) Wang, Y.; Ai, J.; Nie, X.; Li, Z.; Xia, X.; Hussain, T.; Wang, Q.; Wei, Q. Photodynamic Activity Enhanced by In Situ Biosynthetic BC/CQDs@PCN-224 Membranes through FRET Strategy; Carbohyd. Polym. 2023, 307, 120623.

(61) Turan, I.S.; Yildiz, D.; Turksoy, A.; Gunaydin, G.; Akkaya, E.U. A Bifunctional Photosensitizer for Enhanced Fractional Photodynamic Therapy: Singlet Oxygen Generation in the Presence and Absence

of Light Angew. Chem. Int. Ed. 2016, 55, 2875-2878.

(62) Zheng, X.; Zhong, J.; Dong, M.-Y.; Wen, Y.; Chen, A.-Z. Synthesis of Porphyrin-Based 2D Ytterbium Metal Organic Frameworks for Efficient Photodynamic Therapy; RSC Adv. 2022, 12, 34318-34324.

(63) Lu, Z.; Gao, J.; Rao, S.; Jin, C.; Jiang, H.; Shen, J.; Yu, X.; Wang, W.; Wang, L.; Yang, J. A Multifunctional Membrane Based on TiO_2/PCN-224 Heterojunction with Synergistic Photocatalytic-Photothermal Activity under Visible-Light Irradiation Appl. Catal. B-Environ. 2024, 342, 123374.

(64) Li, Z.; Liu, Z.; Ng, T.Y.; Sharma, P. The Effect of Water Content on the Elastic Modulus and Fracture Energy of Hydrogel Extreme Mech. Lett. 2020, 35, 100617.

(65) Mao, C.; Xiang, Y.; Liu, X.; Cui, Z.; Yang, X.; Yeung, K.W.K.; Pan, H.; Wang, X.; Chu, P.K.; Wu, S. Photo-Inspired Antibacterial Activity and Wound Healing Acceleration by Hydrogel Embedded with Ag/Ag@AgCl/ZnO Nanostructures ACS Nano 2017, 11, 9010-9021.

(66) Wang, B.; Xu, Y.; Shao, D.; Li, L.; Ma, Y.; Li, Y.; Zhu, J.; Shi, X.; Li, W. Inorganic Nanomaterials for Intelligent Photothermal Antibacterial Applications Front. Bioeng. Biotechnol. 2022, 10, 1047598.

(67) Wang, Y.; Nie, X.; Lv, Z.; Hao, Y.; Wang, Q.; Wei, Q. A Fast Hemostatic and Enhanced Photodynamic 2-Dimensional Metal-Organic Framework Loaded Aerogel Patch for Wound Management J. Colloid Interf. Sci. 2024, 656, 376-388.

(68) Li, Q.; Hu, E.; Yu, K.; Xie, R.; Lu, F.; Lu, B.; Bao, R.; Dai, F.; Lan, G. Gemini Dressing with both Super-Hydrophilicity and-Hydrophobicity Pursuing Isolation of Blood Cells for Hemostasis and Wound Healing Adv. Fiber Mater. 2023, 5, 1-20.

(69) Peng, X.; Xu, X.; Deng, Y.; Xie, X.; Xu, L.; Xu, X.; Yuan, W.; Yang, B.; Yang, X.; Xia, X. Ultrafast Self‐Gelling and Wet Adhesive Powder for Acute Hemostasis and Wound Healing Adv. Funct. Mater. 2021, 31, 2102583.

(70) Long, M.; Zhang, Y.; Huang, P.; Chang, S.; Hu, Y.; Yang, Q.; Mao, L.; Yang, H. Emerging Nanoclay Composite for Effective Hemostasis Adv. Funct. Mater. 2018, 28, 1704452.

Table Of Contents (TOC)